



**HAL**  
open science

# Controlling the force and the position of acoustic traps with a tunable acoustofluidic chip: application to spheroid manipulations

Nathan Jeger-Madiot, Mauricio Hoyos, Jean-Luc Aider

► **To cite this version:**

Nathan Jeger-Madiot, Mauricio Hoyos, Jean-Luc Aider. Controlling the force and the position of acoustic traps with a tunable acoustofluidic chip: application to spheroid manipulations. 2021. hal-03832185v1

**HAL Id: hal-03832185**

**<https://hal.science/hal-03832185v1>**

Preprint submitted on 26 Nov 2021 (v1), last revised 27 Oct 2022 (v2)

**HAL** is a multi-disciplinary open access archive for the deposit and dissemination of scientific research documents, whether they are published or not. The documents may come from teaching and research institutions in France or abroad, or from public or private research centers.

L'archive ouverte pluridisciplinaire **HAL**, est destinée au dépôt et à la diffusion de documents scientifiques de niveau recherche, publiés ou non, émanant des établissements d'enseignement et de recherche français ou étrangers, des laboratoires publics ou privés.

Cite this: DOI: 00.0000/xxxxxxxxxx

## Controlling the force and the position of acoustic traps with a tunable acoustofluidic chip : application to spheroid manipulations

Nathan Jeger-Madiot, Mauricio Hoyos, and Jean-Luc Aider<sup>a</sup>

Received Date  
Accepted Date

DOI: 00.0000/xxxxxxxxxx

In this study, we present a multi-node acoustofluidic chip working over a large range of frequencies. This approach opens the path to a multitude of acoustophoretic manipulations including the accurate control of the force applied onto cells and cell spheroids, but also the ability to move the levitation nodal planes, the merging and the assembly of spheroids. The design of a transparent cavity and the use of a broadband ultrasonic transducer allow the characterization of the acoustic energy and the comparison with a simple 1D model. The acoustic properties of the system were first estimated through the effects of the acoustic radiation force (ARF) on suspension of particles. From the particles velocities induced by the ARF, measured by Particle Image Velocimetry (PIV), we deduce the acoustic energy over a large frequency range. The automation of the setup allowed the acquisition of a large amount of data with the possibility to make parametric and statistic studies. The results show a wide continuous operating range for the acoustic radiation forces. We also show that it is possible to apply a constant amplitude for the ARF even while changing the acoustic frequency. This approach is applied on human Mesenchymal Stem Cells (hMSCs). We show that it is possible to create large hMSC spheroids on each acoustic node, as demonstrated recently in [Jeger-Madiot *et al.*, *Scientific Reports*, 2021, 11, 8355], before moving and merging them while maintained in acoustic levitation.

### 1 Introduction

The rise of microfluidics together with efficient piezoelectric devices during the last 20 years lead to an increasing interest for acoustofluidics and its applications to acoustophoresis. These approaches have shown many benefits for soft, label-free and non-contact manipulations of particles or biological cells in microfluidic systems<sup>1,2</sup>. This rapidly growing research field addresses many challenges<sup>3,4</sup> in biotechnology, medicine or chemistry. The main principles rely on the interaction between the acoustic waves and the handled objects. Depending on the needs of the application, the acoustic forces can be combined with other forces like flow viscous drag<sup>5</sup>, optical<sup>6</sup> or gravity ones<sup>7</sup>. Acoustophoresis is used as a robust method for concentrating<sup>8–10</sup>, washing<sup>11</sup>, separating<sup>5,12</sup> or trapping<sup>13,14</sup> cells. The most usual devices shape bulk acoustic waves (BAW) in order to obtain standing waves<sup>15–17</sup>.

Because of the issue of the applications, the acoustophoretic tools require a highly accurate characterization of the device. The first key problem, with such systems, relies on the identification of the optimal resonance frequency peak and the estimation of the quality factor  $Q$ . It can be done with electrical methods like

admittance curves<sup>18</sup> or differential impedance measurement<sup>2</sup>. Others approaches used the static mechanic effects on the objects under levitation, such as the equilibrium with the gravitational forces<sup>19</sup>, and the theoretical models<sup>20</sup> to estimate the acoustic pressure. On the other hand, dynamic transient motion of the particle undergoing the acoustic waves provides also accurate estimation of the acoustic pressure or energy. The issue consists in the assessment of the particle movement under the acoustic forces. Barnkob *et al.*<sup>21</sup> developed a particle tracking method to measure the acoustic pressure. Hağsäter *et al.*<sup>22</sup> and Augustsson *et al.*<sup>23</sup> have used micro-particle image velocimetry (PIV) to characterize the acoustic properties of microchannels and Dron & Aider<sup>24</sup> proposed an optical method based on defocused particle image to evaluate the acoustic energy density in the cavity.

Most of the acoustofluidics designs rely on the search of the best fit between the height of the cavity and the acoustic frequency, in order to maximize the ARF. Dron & Aider<sup>25</sup> have shown that acoustofluidic systems still work beyond the resonant frequency, leading to the possibility to change the location of the acoustic levitation plane just by tuning the acoustic frequency. This was made possible because of the use of a broadband acoustic transducer and a multi-layer device, as suggested by Hill *et al.*<sup>26</sup>. The present work goes further and generalize the first discovery to multi-node devices with a proper theoretical framework.

<sup>a</sup>Laboratoire de Physique et Mécanique des Milieux Hétérogènes (PMMH), UMR 7636 CNRS, ESPCI Paris, PSL, Paris Sciences et Lettres University, Sorbonne Université, Université de Paris 1, Paris, 75005, France; E-mail: nathan.jeger-madiot@espci.fr

In this study, we focus on the design of a standing-wave cavity with several acoustic nodes. The geometry of the microfluidic chip and the broadband transducer allow the particle manipulation over a large range of frequencies. The working setup is explained with a plain theoretical approach, and with the measurement of the focusing particle velocities over a larger frequency spectrum. We show that the acoustic levitation is at least effective from 1.5MHz to 2.5MHz. The trapped particles can be continuously moved from a position to another in a stable way.

To show the large potential of this approach, we applied this approach to human Mesenchymal Stem Cells (hMSCs). After a first step, lasting ten hours, consisting in the self-organization of the hMSCs into spheroids in acoustic levitation<sup>13</sup>, we were able to move the spheroids closer to each other in a stable way just by tuning the frequency, before finally merging them. This original approach opens the path to the scaffold-free creation and culture of assembloids and organoids of various cellular type, in acoustic levitation.

## 2 Background theory

In this section, we first describe the basic theory of acoustics for a one-dimensional model. From the knowledge of the acoustic field properties in the cavity, we can deduce the different forces acting on small particles or cells. All these properties will then be experimentally estimated using a  $\mu$ PIV method.

### 2.1 Acoustic resonance in a multilayered device

In our system, the dimension of the transducer and the cavity are very large in comparison to the wavelength ( $r_{trans} = 4\text{mm} \gg \lambda_{2\text{MHz}} \approx 0,75\text{mm}$ ) so we can consider plane wave emission and reflection and the use of a 1D model to describe the physic phenomenon<sup>27</sup>. It is only adapted to the axial component of the ARF, the transverse component being associated to radial gradient of the acoustic field. In our device, the vibrating emitting surface is directly in contact with the suspending medium, i.e. there is no transmitting layer. In this case, three layers are modeled: the water medium in which the particles are floating, the glass slide, opposite to the acoustic source, acting as the acoustic reflector and the semi-infinite medium, on the other side of the reflecting lay, modeled as a simple air layer (Fig. 1).

The classical equations of linear acoustics<sup>28</sup> can be applied in the material (n) considering a harmonic plane wave with the following parameters: the angular frequency  $\omega = 2\pi f$ , the wave number  $k_n = \frac{2\pi}{\lambda_n} = \frac{\omega}{c_n}$ , the longitudinal sound celerity  $c_n$  and the density of the materials  $\rho_n$ . The acoustic velocity and pressure can be expressed as follows:

$$\begin{cases} v_n(x, t) = A_n e^{-j(\omega t - k_n x)} + B_n e^{-j(\omega t + k_n x)} \\ p_n(x, t) = \rho_n c_n (A_n e^{-j(\omega t - k_n x)} - B_n e^{-j(\omega t + k_n x)}) \end{cases} \quad (1)$$

with  $A_n$  the velocity amplitude of the progressive propagating wave and  $B_n$  the velocity amplitude of the regressive propagating wave ( $n = 1, 2$  or  $3$ ).

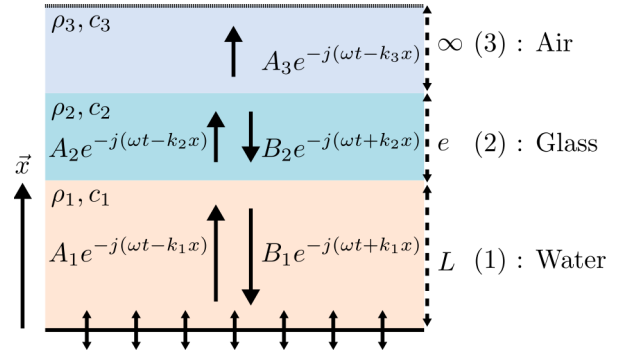


Fig. 1 Sketch of the three layers model (not to scale). The transducer is modeled by a vibrating surface directly in contact with the water medium. A glass slide, inserted between the cavity water and the air semi-infinite medium, reflects the acoustic wave. Two interfaces are considered: the water/glass and the glass/air interfaces.

The surface transducer vibrates with the following velocity:

$$v(t) = v_{source} e^{-j\omega t} \quad (2)$$

$v_{source}$  being the velocity amplitude of the transducer. It can be linked to the displacement amplitude  $\delta$  by  $v_{source} = \omega\delta$ .

The regressive wave appears from the impedance mismatch between two mediums. To determine the acoustic velocity and pressure in the material (n), the boundary conditions are used. At each interface, the normal acoustic velocity and the pressure are continuous:

$$\begin{cases} v_1(0, t) = v_{source} e^{-j\omega t} \\ v_1(L, t) = v_2(L, t) \\ p_1(L, t) = p_2(L, t) \\ v_2(L + e, t) = v_3(L + e, t) \\ p_2(L + e, t) = p_3(L + e, t) \end{cases} \quad (3)$$

To calculate the coefficients  $A_n$  and  $B_n$ , the definitions of  $v_n$  and  $p_n$  (Eq. 1) are introduced in the set of boundary conditions defined in Eq. 3. The resulting equation system is then solved with the matrix formulation given by Folds & Loggins<sup>29</sup>:

$$\begin{bmatrix} A_1 \\ B_1 \\ A_2 \\ B_2 \\ A_3 \end{bmatrix} = M^{-1} \begin{bmatrix} v_{trans} \\ 0 \\ 0 \\ 0 \\ 0 \end{bmatrix} \quad (4)$$

The coefficients of the matrix  $M$  are the following:

$$\begin{aligned} \langle v^2 \rangle &= \frac{1}{2} v_m^2 \cos(kx + \phi)^2 \\ \langle p^2 \rangle &= \frac{1}{2} (\rho_w c_w v_m)^2 \sin(kx + \phi)^2 \\ \frac{\partial \langle v^2 \rangle}{\partial x} &= v_m^2 (-k) \sin(kx + \phi) \cos(kx + \phi) \\ \frac{\partial \langle p^2 \rangle}{\partial x} &= (\rho_w c_w v_m)^2 k \cos(kx + \phi) \sin(kx + \phi) \end{aligned} \quad (5)$$

and can be calculated with the settings of the experience. For an invertible matrix  $M$ , the acoustic velocity and pressure can be estimated. The results are given in the experimental section.

## 2.2 Acoustic energy density

For a 1D model considering plane waves, the acoustic energy density  $w$  can be expressed by the sum of the acoustic potential energy density  $e_k$  and the kinetic one  $e_p$ :

$$w(x,t) = e_k(x,t) + e_p(x,t) = \frac{1}{2}\rho_n v_n(x,t)^2 + \frac{1}{2\rho_n c_n^2} p_n(x,t)^2 \quad (6)$$

This energy density  $w$  describes the energy stored by the fluid molecules, per volume unit, and is a function of time  $t$  and of space  $x$ . Its unit is  $J/m^3$ . Usually, we use a global acoustic energy density averaged in time and in space, to describe the cavity:

$$E_{ac} = \frac{1}{L} \int_0^L \frac{1}{T} \int_0^T w(x,t) dt dx \quad (7)$$

with  $L$  the height of the cavity,  $T = \frac{1}{f}$  the period of the wave.

As  $\langle \cos(\omega t)^2 \rangle = \langle \cos(kx)^2 \rangle = \frac{1}{2}$ , the global energy acoustic density can be calculated theoretically using Eq. 6 and Eq. 7:

$$E_{ac} = \frac{1}{2}\rho_n v_m^2 \frac{1}{4} + \frac{1}{2\rho_n c_n^2} \frac{1}{4} (\rho_n c_n v_m)^2 = \frac{1}{4}\rho_n v_m^2 \quad (8)$$

## 2.3 The acoustic radiation forces (ARF) on small particles

The creation of an acoustic standing wave inside a resonant cavity leads to interactions with the particles suspended in the inviscid fluid. The scattering of the acoustic wave on a particle results in the creation of the Acoustic Radiation Force (ARF) which depends on the magnitude and frequency of the acoustic wave and on the particle properties. Bruus & al. al.<sup>20,28</sup> studied and explained perfectly well the origins of this force. The ARF results from the time-averaged force exerted on a particle due to the scattering of the acoustic waves from the particles<sup>30</sup>. This force was first studied by King<sup>31</sup> for incompressible spheres, then Yosioka & al.<sup>32</sup> took into account the compressibility of the particles. Finally the ARF on particles was generalized by Gor'kov<sup>33</sup>. The domain of validity is limited to particles with a diameter  $d_p$  much smaller than the acoustic wavelength  $\lambda_{ac}$  (Rayleigh hypothesis). In this work, we used  $15\mu m$  particles, so the theory is valid for frequencies smaller than  $f_c < \frac{c}{\lambda_c} = \frac{c}{10d_p} \approx 10MHz$ . In the general case, the ARF can be expressed<sup>28</sup> as:

$$F^{rad} = \frac{4\pi}{3} r_p^3 \frac{\partial}{\partial x} \left\{ \frac{1}{2} \left( \frac{1}{\rho_w c_w^2} - \frac{1}{\rho_p c_p^2} \right) \langle p^2 \rangle - \frac{3}{2} \frac{\rho_p - \rho_w}{2\rho_p + \rho_w} \rho_w \langle v^2 \rangle \right\} \quad (9)$$

with  $r_p$  the particle radius,  $\rho_w$  the water density,  $c_w$  the ultrasound longitudinal velocity in water,  $\rho_p$  the particle density,  $c_p$  the ultrasound velocity in the particle,  $\langle p \rangle$  the time-averaged acoustic pressure and  $\langle v \rangle$  the time-averaged acoustic velocity.

## 2.4 The standing wave resonator

The reflection of the wave on the water-glass interface generates a standing wave in the cavity. The resulting acoustic field can be decomposed as the superposition of a standing wave and a prop-

agative wave. The contribution of the propagative wave is due to the transmission into the glass medium. We consider that the ARF acting on the particles is mainly due to the standing wave. If we neglect the propagative part, the standing acoustic velocity and pressure can be written:

$$\begin{cases} \vec{v}(x,t) = v_m \cos(kx + \phi) \cos(\omega t) \vec{x} \\ p(x,t) = \rho_w c_w v_m \sin(kx + \phi) \sin(\omega t) \end{cases} \quad (10)$$

with  $v_m$  the magnitude and  $\phi$  the phase, depending on the boundary limits.

From the Eq. 9, we calculate the ARF for a standing wave:

$$F^{rad} = 4\pi r_p^3 \beta k E_{ac} \sin(2kx + 2\phi) \quad (11)$$

$\beta$  is the acoustic contrast factor given by:

$$\beta = \frac{\rho_p + \frac{2}{3}(\rho_p - \rho_w)}{2\rho_p + \rho_w} - \frac{\rho_w c_w^2}{3\rho_p c_p^2} = \beta_d + \beta_c \quad (12)$$

The acoustic contrast factor is decomposed as the sum of the density ratio  $\beta_d$  and the compressibility ratio  $\beta_c$ . If  $\beta > 0$  (resp.  $\beta < 0$ ), the particles will move toward the pressure node (resp. antinode).

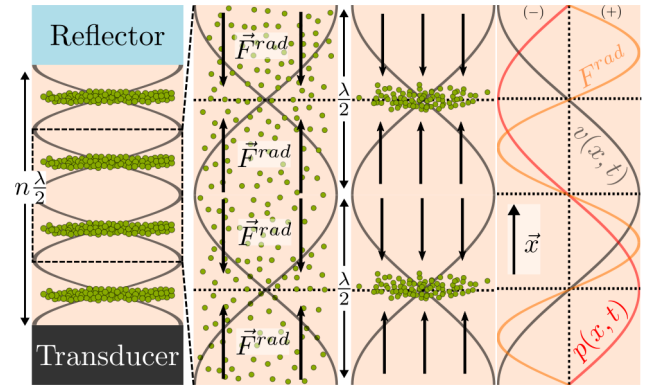


Fig. 2 Sketch of the multi-nodes cavity in the resonance configuration: the cavity height must match an integer of the half acoustic wavelength (figure on the left). The three figures on the right side are a zoom around the two central pressure nodes shown on the left. The ARF pushes the particles (if  $\beta > 0$ ) toward the pressure node. The particles are then trapped into the acoustic levitation planes. The ARF is modulated with a spatial period two times smaller than the acoustic pressure and velocity. The pressure and the velocity are in a phase quadrature.

## 2.5 Link between the ARF and the particle track

The purpose of this section is to link the motions of the particles to the acting forces. According to the Newton's second law, we can write:

$$m\vec{a} = \sum \vec{F} = \vec{F}^{buo} + \vec{F}^{rad} + \vec{F}^{sto} \quad (13)$$

where  $\vec{F}^{buo}$  is the buoyancy force,  $\vec{F}^{rad}$  is the acoustic radiation force and  $\vec{F}^{sto}$  is the viscous Stokes drag force.

For  $15\mu m$  polystyrene beads, the buoyancy force is:

$$F^{buo} = \frac{4\pi}{3} r_p^3 (\rho_f - \rho_p) g \approx 7.10^{-12} N \quad (14)$$

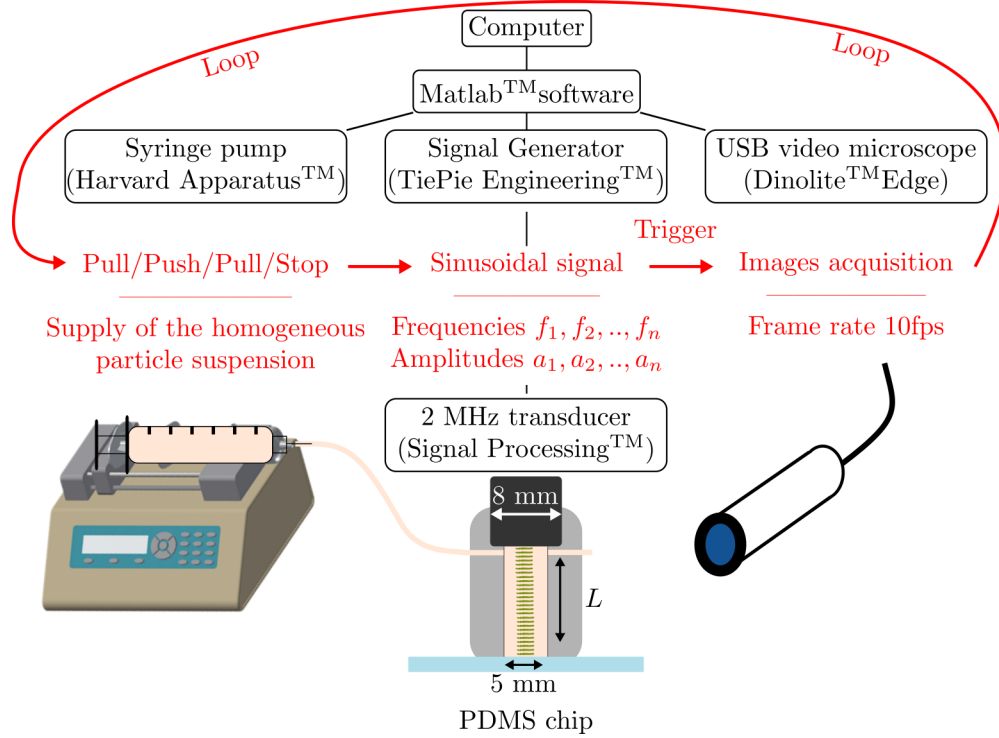


Fig. 3 Schematic of the experimental setup. A laptop with Matlab™ software controls the whole chain. The first step consists in supplying the cavity with an homogeneous particle suspension. The syringe pump produces goings and comings to reorganize the previous particle aggregate into an homogeneous particle suspension inside the cavity. The ultrasound transducer is turned on simultaneously with the images sequence acquisition. It works with a closed loop and it allows the possibility to repeat the same experience and make a parametric study. We study here the effect of a frequency variation.

and can be neglected.

According to previous works<sup>21,23,28</sup>, if the motion of the particle is slow and if the particle is small, the inertial effects can safely be neglected. The particle path can then be deduced from the balance between the ARF  $\vec{F}^{rad}$  and the Stokes force  $\vec{F}^{sto}$ . Using Eq. 11 and the standard expression for the Stokes force applied on a sphere  $\vec{F}^{sto}$ , we obtain:

$$\vec{0} = \vec{F}^{rad} + \vec{F}^{sto} = \left( 4\pi r_p^3 \beta k E_{ac} \sin(2kx + 2\phi) - 6\pi \eta r_p V_p \right) \vec{x} \quad (15)$$

with  $r_p$  the particle radius,  $\beta$  the acoustic contrast factor,  $k$  the acoustic wavenumber,  $E_{ac}$  the acoustic energy density,  $\eta$  the dynamic viscosity and  $V_p$  the particle velocity.

Thus, from the equality (15) we can determine the acoustic energy density  $E_{ac}$  or the ARF  $F^{rad}$  from the observation and the calculation of the particle velocity. The movement velocity of the particles must fit the following sinusoidal shape:

$$v_p(x) = \frac{2\beta r_p^2 k E_{ac}}{3\eta} \sin(2kx + 2\phi) \quad (16)$$

By taking the magnitude of  $V_p$  we can estimate  $E_{ac}$ :

$$E_{ac} = \frac{3\eta}{2\beta r_p^2 k} |V_p(x)| \quad (17)$$

Measuring the velocity magnitude gives then an easy access to the mean acoustic energy.

## 3 Materials and methods

### 3.1 Experimental setup

The setup has been designed to be fully automated, in order to carry out easily a large parametric study. Every devices can be controlled by a computer and can work in closed-loop (Fig. 3). The syringe pump (Harvard Apparatus™) supplies the homogeneous particles suspension by alternatively pushing and pulling the medium. Once the fluid has settled, the ultrasound transducer (SignalProcessing™) and the USB digital microscope are simultaneously triggered. The possibility to control each parameter of the setup allows the acquisition of a large amount of data in a relatively short time, about one hour for the settings used here.

The ultrasonic transducer is powered by an arbitrary waveform generator (Handyscope HS5 from Tiepie Engineering™). An USB digital microscope (Edge from Dinolite company™) capture sequences of images with a framerate equal to 45 fps. The flow rates used to mix the particles in a suspension are 5mL/min. We used polystyrene particles (Phosphorex™) with a diameter of 15μm.

### 3.2 Acoustofluidic chip

The chip is made of a PDMS (Polydimethylsiloxane, RTV 615, Neyco™) body bonded on a microscope cover-glass and a mono-element ultrasonic transducer.

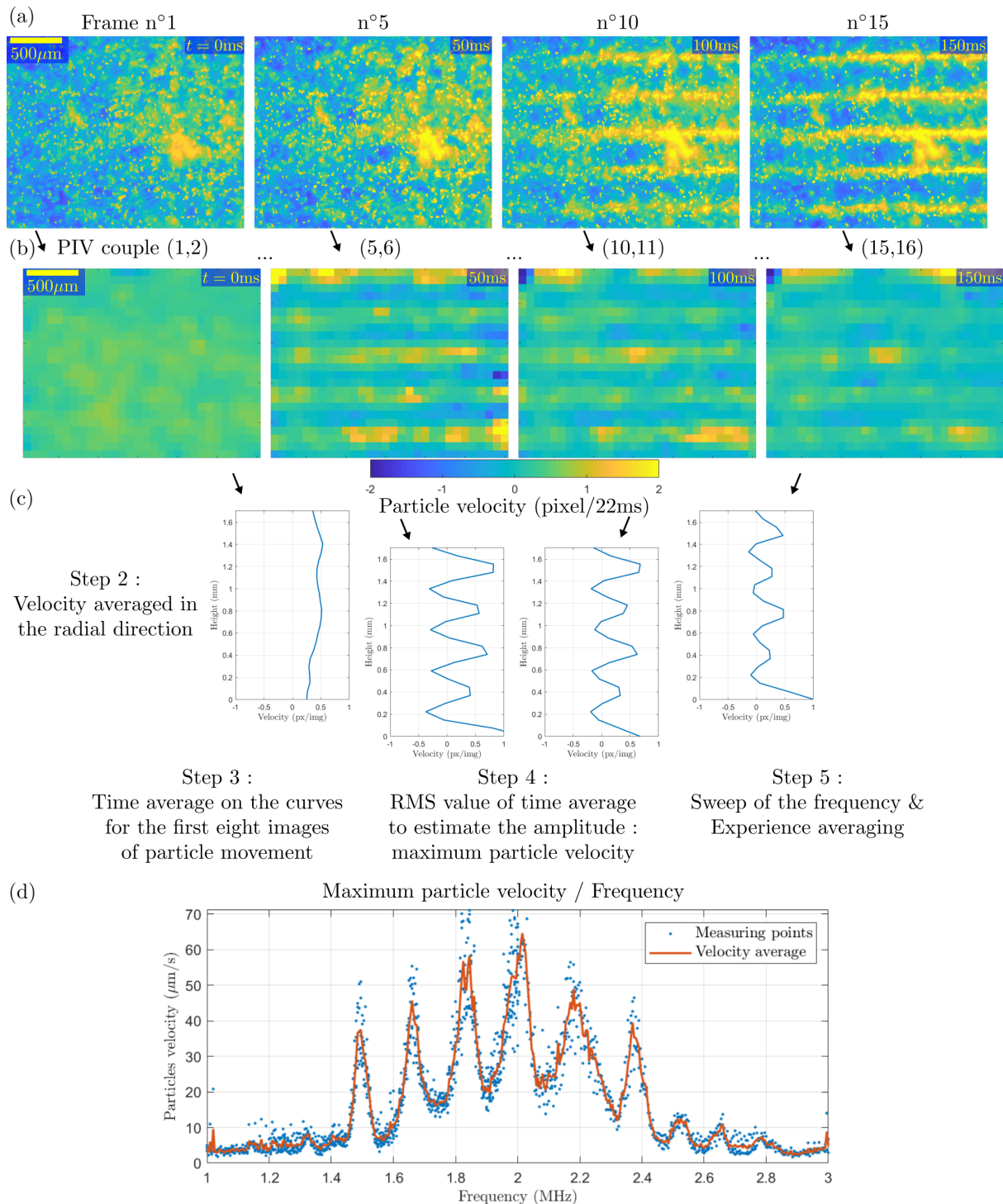


Fig. 4 (a) 8-bits grayscale snapshots acquired with the USB video microscope on the side of the resonant cavity (side-view). The frame rate is about 45fps. It illustrates the acoustic focusing process from  $t = 0$  (no US) to  $t = 350ms$  (particles focused in the levitation planes) (b) PIV images obtained with PIVlab from the snapshots time-serie. (c) Post-processing steps. The PIV fields are spatially averaged along the radial direction, leading to vertical profile of axial focusing velocity. From this velocity profile, the amplitude of the velocity is derived. The final step consists in varying the acoustic frequency to evaluate the evolution of the particle velocity as a function of the acoustic frequency. (d) Evolution of the particle focusing velocity as a function of the acoustic frequency. Six large peaks of the maximum axial velocity can be seen in the frequency band ranging from 1.4 to 2.4 MHz.

The geometry of the PDMS chip is designed to allow the insertion of the ultrasonic transducer inside the PDMS body, which closes the acoustofluidic cavity. One side of the resonant cavity is the ultrasound emitter, in contact with the fluid, avoiding acoustic losses through various interfaces, while on the other side the microscope cover-glass acts as a powerful acoustic reflector and allows a transparent optical access. The overall acoustic resonant cavity is simple and efficient.

To shape the PDMS body, we use a negative mold made with a 3D printer (3D Form 2 from Formlabs Inc.<sup>TM</sup>). The PDMS is poured inside the mould and put in an oven at 70°C for 24h.

The overall dimensions of the resonant cavity are its diameter  $d = 5$  mm and its height  $h$ . In the following, we will use multi-nodes cavity, i.e.  $h = N \frac{\lambda}{2}$ , with  $N > 1$ .

### 3.3 Transducer characterization

The necessary condition to make a broadband multi-node chip relies on the use of a large bandwidth ultrasonic transducer. To explain the next results, we have experimentally characterized the transducer by using self-reciprocity methods<sup>34,35</sup>. The principle<sup>36</sup> of these approaches uses the double reciprocity of the transducer which can both emit or receive signal. We assume that the transfer function  $h(t)$  of the transducer is the same for the emission and the reception. At first approximation, we neglected the wave diffraction. By emitting a pulse signal on a reflective wall, we can measure the frequency response  $H_{transducer}(f)$  of the transducer with the received signal. The electrical received signal  $r(t)$  is expressed :

$$r(t) = e(t) * h(t) * h(t) \quad (18)$$

with  $e(t)$  the electrical emitted signal,  $*$  the convolution product and  $h(t)$  the impulse response of the transducer. Passing in the Fourier transform domain, we finally find the frequency response of the transducer  $H_{transducer}(f)$ :

$$H_{transducer}(f) = \sqrt{\frac{R(f)}{E(f)}} \quad (19)$$

with  $E(f)$  the Fourier transform of the emitted signal  $e(t)$ ,  $R(f)$  the Fourier transform of the received signal  $r(t)$ . To cover the interesting bandwidth, one sinusoidal period with the carrier frequency of 2MHz was emitted. The result is shown on Fig. 5.

### 3.4 $\mu$ PIV method

In order to estimate the particle velocity, a micro Particle Image Velocimetry ( $\mu$ PIV) method is used. PIV is a measurement technique used to measure velocity fields through the displacements of particles between two successive snapshots.

The principle consists in computing the cross-correlation between two successive snapshots which are divided into interrogation windows (IW). The cross-correlations are computed over each IW, leading to one velocity vector per IW. To manage our data, we have used the PIVlab software on Matlab<sup>TM</sup>, developed by W. Thielicke<sup>37,38</sup>.

From the movies of the transient focusing (Fig. 4(a)) of parti-

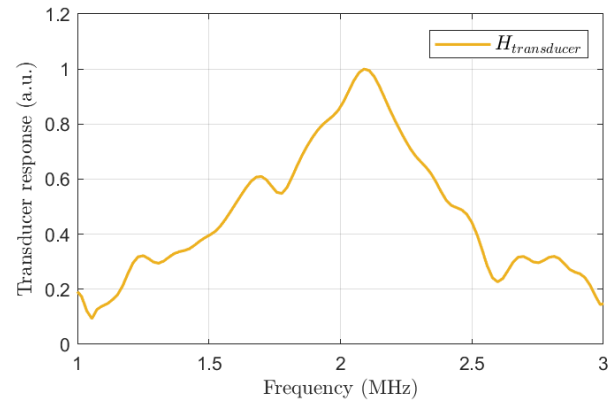


Fig. 5 Estimation of the transducer frequency response  $H_{transducer}(f)$  with the self-reciprocity method.

cles toward the acoustic nodes, we extract the map of velocities (Fig. 4(b)) using PIVlab. We used an IW size of 64 pixels for the first pass. The second pass used a 32 pixel IW. In both cases we used a 50% overlap to increase the spatial resolution. No intensity threshold or pre-processing was applied to the raw images.

### 3.5 Parametric study of the axial velocity

The  $\mu$ PIV measurements gives us access to the axial acoustic focusing velocity profile along the vertical axis of the acoustic chamber, which means the focusing velocity towards multiple pressure nodes. With the determination of the particle velocity maxima along the  $x$  axis, we can deduce the ARF  $x$ -profile and then the acoustic energy as a function of the frequency.

The main steps are summarized on Fig. 4. First, from the 8-bits gray-scale images (Fig.4(a)), the instantaneous PIV fields are calculated (Fig. 4(b)). Before the triggering of the acoustic emission, the axial velocity is almost null (Fig. 4(b), first field on the left). The velocity is not null because the particles are still in motion after their injection into the cavity. Once the ultrasounds are turned-on, the PIV fields show quickly the expected sinusoidal pattern along the axial direction (Fig. 4(b),  $t = 50$  ms). The whole velocity field is spatially averaged along the radial direction to obtain axial profiles of axial velocity (Fig. 4(c)). Then, the first eight velocity profiles following the acoustic trigger are selected and averaged in time (step 3). Finally, we estimate the velocity maximum by calculating the root mean square value (RMS) weighted by  $\sqrt{2}$  over the time-averaged velocity profile (step 4). This process is then applied systematically for a parametric study of the maximum velocity as a function of the acoustic frequency over a wide frequency range ( $1 \leq F_{ac} \leq 3$  MHz). We show on Fig. 4(d) a typical example of the evolution of the maximum axial velocity of the particles as function of the acoustic frequency. As expected, one can see clear and sharp maxima corresponding to the acoustic resonances found when changing the number of pressure nodes.

### 3.6 Estimation of the node position

Another interesting feature is to measure the axial location  $z_{foc}$  of the pressure nodes as a function of the acoustic frequency. One can expect that it will also depends on  $F_{ac}$ , as previously observed in a single node acoustic trap<sup>25</sup>.

In order to estimate the position of the nodes, we are no longer interested in the transient steps of acoustic focusing. We need stable acoustic levitation planes. For this reason, the first step consists in forming stable aggregates over the full height of the cavity. Then, we sweep the acoustic frequency from 1.7MHz to 2.5MHz. Simultaneously the camera records the evolution of the aggregates positions. We then select the correct region of interest, before applying a projection in the radial direction by selecting the maximum intensity of the pixels at each axial position leading to the axial locations of each aggregate.

### 3.7 Estimation of the spheroid positions

In order to characterize the evolution of the positions of the spheroids with the frequency shift, we developed a Matlab image analysis code. It works automatically with a few user-defined parameters. In particular, we manually defined the regions of interest (ROIs) for each spheroid. Then an ellipsoid is fitted on the binarized image. The position of the ellipse center provided the global heights of the spheroids on the image. For the whole image sequence, ROIs were defined automatically from the ellipsoid characteristics of the previous image. We obtained the frequency evolution of the axial positions of the spheroids.

### 3.8 MSC isolation and characterization

MSCs were isolated from adipose tissue of the thigh of a healthy donor, after a signed consent, according to the French regulations. MSCs were obtained after the digestion of adipose tissue with collagenase NB6 (SERVA ELECTROPHORESIS, Heidelberg, Germany). The adipose tissue was placed in 40 ml of collagenase NB6 diluted in  $\alpha$ -MEM medium at a final concentration of 5  $\mu$ g/ml in a 50 ml conical tube (Falcon, Dutscher, Bernolsheim, France). After a 2 hours incubation at 37°C, the digested tissue was filtered through a cell strain with pores of 100  $\mu$ m to remove the remaining tissues. The strained cells were then centrifuged and plated in a cell factory (THERMOFISHER, NUNC, Waltham, United States) for expanding in MSC culture medium composed of  $\alpha$ -MEM (GIBCO, THERMOFISHER, Waltham, United States) supplemented with 10% fetal bovine serum (FBS, BIOWEST, Nuaillé, France) and 1% antibiotic / antimycotic mix (Anti-Anti 100x, GIBCO, THERMOFISHER, Waltham, United States).

## 4 Results

In the following we will consider two different heights for the cavity:  $h = 4$ mm and  $h = 10$ mm.

### 4.1 Evolution of the acoustic energy over a broadband spectrum for $h = 4$ mm

From the particles velocity, we deduce the ARF magnitude by using Eq. 15. The particle velocity and the ARF magnitude are related by the proportional coefficient ( $-6\pi\eta r_p$ ). We observe sev-

eral resonance peaks for increasing acoustic frequency. Each peak corresponds to the creation of a new node in the acoustic cavity. One can also see that the velocity is maximum for  $F_{ac} = 2$  MHz, which corresponds to the optimal resonant frequency of the acoustic transducer. The measurement is highly reproducible with a small standard deviation ( $\overline{SD} = 3.35 \pm 3.15 \mu\text{m/s}$ ).

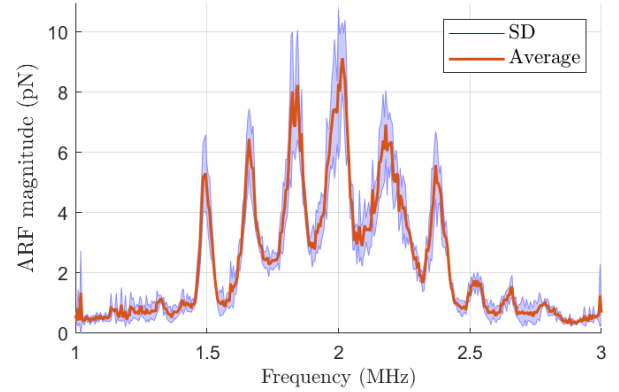


Fig. 6 The ARF magnitude is plotted as a function of frequency. The average and the standard deviation of the measurement are presented.

The prior knowledge of the particle properties allows to estimate the acoustic energy density ( $E_{ac}$ ) (Fig. 7) with the Eq. 17. For the frequencies ranging from 1.5 MHz to 2.75 MHz, one can see multiple maxima with the maximum values of the acoustic energy density reaching 1,5  $\text{J/m}^3$ . Nevertheless, at the anti-resonance the acoustic focusing is still working with an energy density about 0,5  $\text{J/m}^3$ , only three times lower than the maximum found at the resonance. The resonance peaks of the cavity are narrow and the resonance frequencies can clearly be identified.

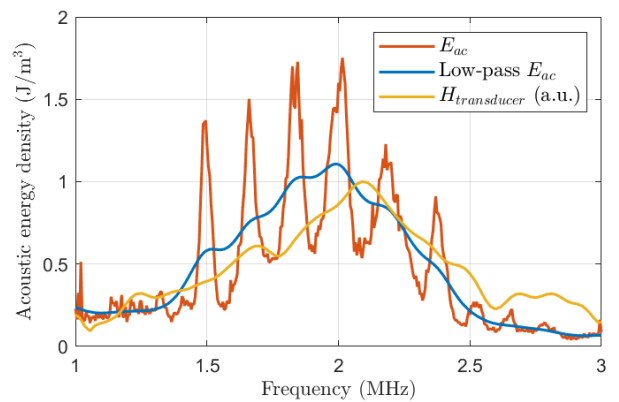


Fig. 7 Estimation of the acoustic energy density as a function of the frequency. The acoustic energy density (red curve) has been calculated from the particle velocity (Fig. 6 and by using Eq. 17). To highlight the broadband of the system, the acoustic energy density signal has been low-pass filtered (blue curve) and compared to the frequency response of the transducer (yellow curve in an arbitrary unit).

The comparison between the acoustic energy density given by the experiments and the theoretical 1D model (Fig. 8) shows a



very good agreement for the resonance peaks positions. However, we denote a mismatch with the envelop of the curves. This difference can be explained by the characteristic of the acoustic source. Indeed we use a packaged wide-band ultrasonic transducer which has its own energy distribution as a function of the acoustic frequency (see yellow curve on the Fig. 7). The maximum is obtained at the resonant frequency of this 2 MHz transducer nearby the maximum of the frequency response of the transducer obtained with the self-reciprocity method (see section 3.3).

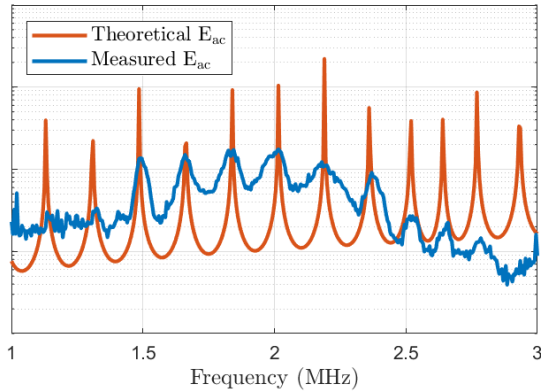


Fig. 8 Comparison of the acoustic energy density  $E_{ac}$  estimated through experimentation with the theoretical 1D model.

The actual height of the cavity can also be checked by comparing the frequency shift between two maxima found with the model and the ones calculated from the experiment. On the Fig. 9 we vary the input height in the model. By minimizing the mean error we determine the height. In this case, the cavity height is estimated at  $h = 4.2$  mm.

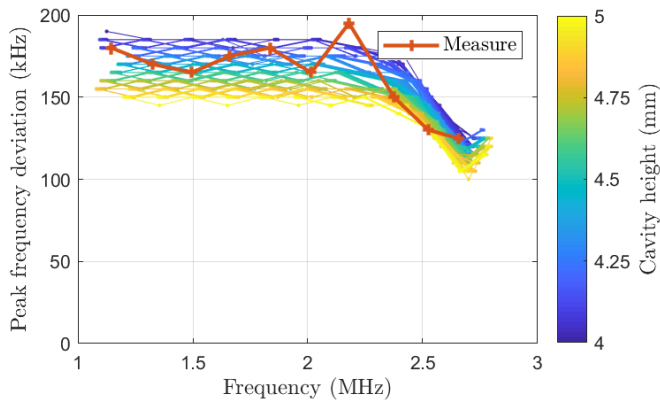


Fig. 9 Comparison of the frequency inter-spaces calculated with the theoretical model for different heights and the ones given by the PIV experiment.

#### 4.2 Estimation of the acoustic energy on a broadband spectrum for $h = 10$ mm

We applied the same process to a higher cavity ( $h = 10$ mm). The acoustic energy density is shown on Fig. 12. As for the 4 mm cavity, the distribution of the energy spreads from 1.5 MHz to

2.75 MHz. The minima of  $E_{ac}$  are the same as in Fig. 7. The main difference is the frequency band between the resonance peaks. As expected by the theory, the number of resonance peaks increases with the height of the cavity, for the same frequency band.

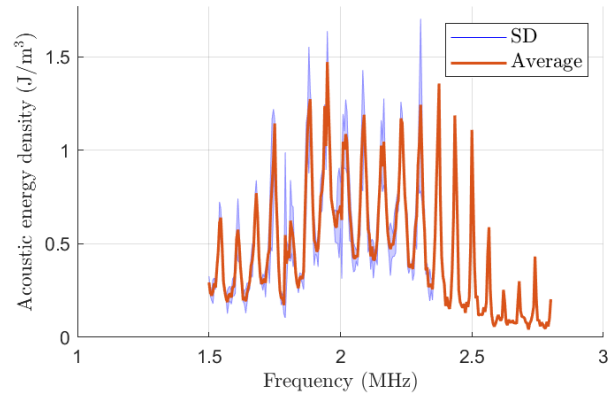


Fig. 10 Estimation of the acoustic energy density for a cavity height about  $h = 10$ mm. The acoustic energy density has been calculated from the particle velocity (Fig. 6 and by using the Eq. 17).

The frequency inter-spaces can also be compared to the theoretical model. By fitting the measured peak to the theoretical 1D model (Fig. 11), we estimate the height to  $h = 11.0$ mm.

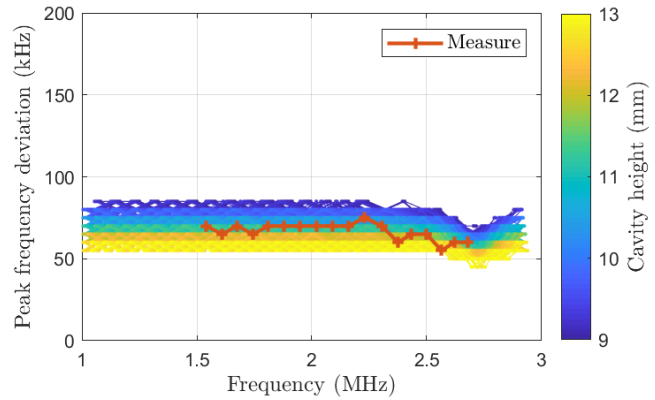


Fig. 11 Comparison of the frequency inter-spaces calculated with the theoretical model for different heights and the ones given by the PIV experiment.

#### 4.3 Evolution of the axial node positions as a function of the frequency

Another interesting feature of the setup is that the axial positions of the aggregate can be varied continuously using the acoustic frequency as a control parameter. Indeed, the Fig. 7 and Fig. 12 show that the acoustic energy remains significant between the resonance peaks, instead of vanishing as one could expect. The consequence is that the levitation planes can be moved smoothly nearly over the entire height of the cavity, from one resonance frequency to the other, just by tuning the acoustic frequency. This is illustrated on Fig. 12, where the axial positions of the aggregates measured experimentally perfectly fit the positions found by the

theoretical 1D model. The relation between the node positions and the frequency is not linear and depends on the axial position of the aggregate. In this experiment we find an amplitude for the axial displacement about  $920 \mu\text{m}$  for the upper node and about  $170 \mu\text{m}$  for the lower node, for a frequency ranging from 1.7 MHz to 2.5 MHz.

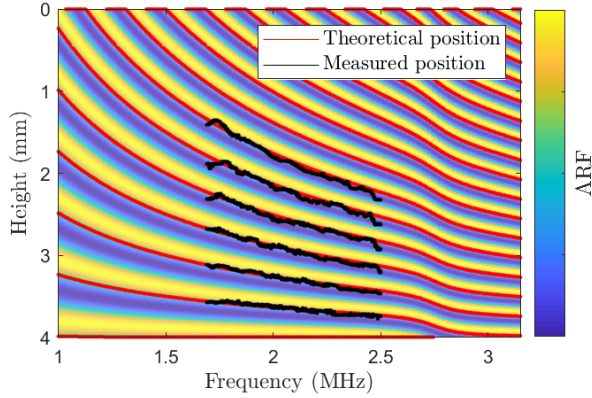


Fig. 12 Comparison between the theoretical and experimental axial positions of the nodes for increasing acoustic frequency. The black lines correspond to the experimental measurements. The contour plot shows the amplitude of the ARF as a function of the frequency and the axial position.

## 5 Manipulation of cell spheroids

In this section, we address a major issue in the modern biology with our approach<sup>39,40</sup>: the manipulation of cell spheroids inside the cell-culture chip. The protocol used by Jeger-Madiot *et al.*<sup>13</sup> was applied to form spheroids with human Mesenchymal Stem Cells (hMSCs) in acoustic levitation. After about ten hours the monolayers of hMSCs spontaneously self-organized into spheroids, as shown in<sup>13</sup>. Once the spheroids are formed, different manipulations can be applied. The position of the spheroids and the distance between them can be controlled.

### 5.1 Control of the axial position

As previously shown with the particles, cell spheroids can be moved just by varying the acoustic frequency. This manipulation is showed on the Fig. 13 where the acoustic frequency varies from 1.94 MHz to 2.3 MHz. The upper spheroid moves from an axial position about  $z = 0.14\text{mm}$  to  $z = 1.10\text{mm}$  and the lower one from  $z = 3.65\text{mm}$  to  $z = 3.95\text{mm}$ , which corresponds respectively to a displacement about  $2.67\text{mm/MHz}$  and  $0.83\text{mm/MHz}$ . The average distance between two spheroids moves from  $39 \mu\text{m}$  to  $32 \mu\text{m}$  which corresponds to a decrease of  $20 \mu\text{m/MHz}$ .

### 5.2 Control of the axial ARF: isoforce displacement

For a given setup, the characterization of the forces in the acoustic cavity provides the predefined pattern of the applied forces as a function of the frequency and the amplitudes of the generator signal. Using this knowledge, it becomes possible to handle the spheroids with a constant amplitude ARF.

For a given configuration, we made a parametric study on the

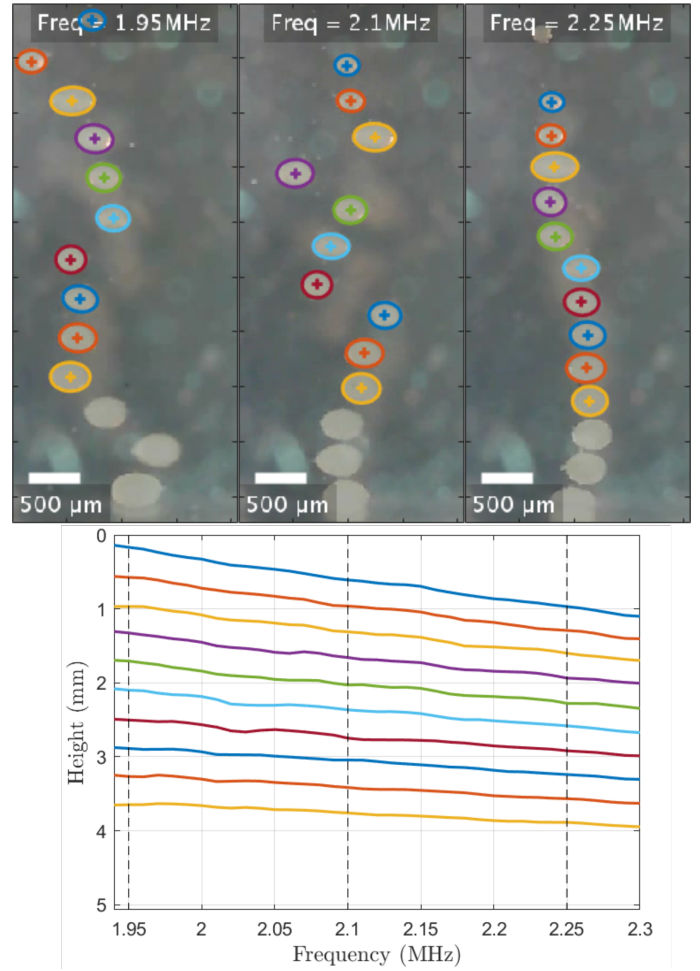


Fig. 13 Control of the spheroids axial positions by varying the acoustic frequency between 1.94 MHz and 2.3 MHz. This manipulation is reversible. Reducing the distance between two spheroids allows their merging. See also the supplementary video 1.

frequency and the amplitude to obtain the signature of the acoustic cavity (Fig 14(a)). To limit the amount of data we arbitrary chose a limited range of frequencies [ $2 - 2.085 \text{ MHz}$ ] and [ $5 - 10 \text{ V}$ ] for the amplitudes. A parabolic dependence between the ARF amplitude and the acoustic frequency can be derived for various voltages applied to the transducer (Fig 14(b)):

$$ARF(f) = a(f)V^2$$

With  $f$  the frequency, and  $a(f)$  the resonance coefficient depending on  $f$ .

Finally, the use of a couple of values frequency-amplitude allow the displacement spheroids with the same ARF magnitude (Fig 14(c)).

### 5.3 Assembly of two spheroids

One of the possible applications of this technology is the merging of two or several cells spheroids. After the first step of self-organization of the spheroids, it is possible to bring them closer and closer. This manipulation promotes the interaction between

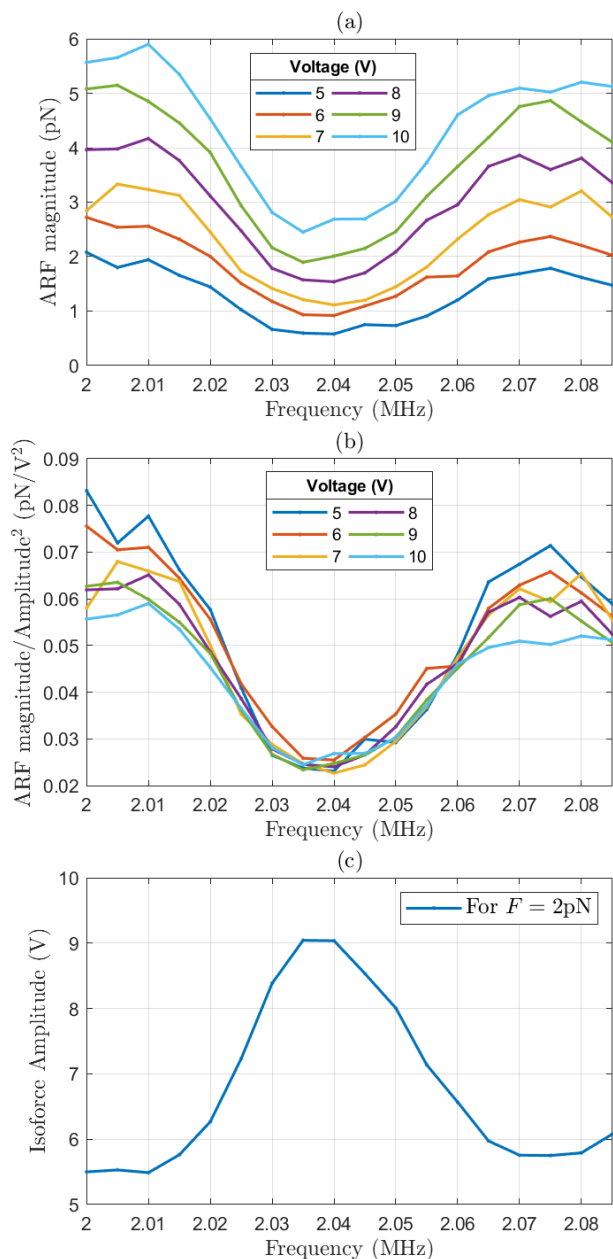


Fig. 14 Estimation of the isoforce voltage amplitude to move spheroids with a constant ARF magnitude. (a) Measure of the magnitude ARF on the range [2 – 2.085MHz] for input voltage from 5V to 10V. (b) Normalization by the square voltage amplitude. (c) From the average of the previous curves, we deduce the voltage amplitude needed to stabilize the applied ARF on spheroids to  $F = 2$  pN.

the spheroids. On the Fig. 15, the spheroids are brought closer to each other. After 16h, the two central spheroids begin to interact and to finally merge. One hour later, an assembloid composed with two spheroids was trapped in acoustic levitation.

## 6 Conclusion

We have presented an automated experimental set-up for the characterization on a large frequency bandwidth of the acoustic energy density in a standing-wave cavity.

The easy implementation and the high reproducibility of this

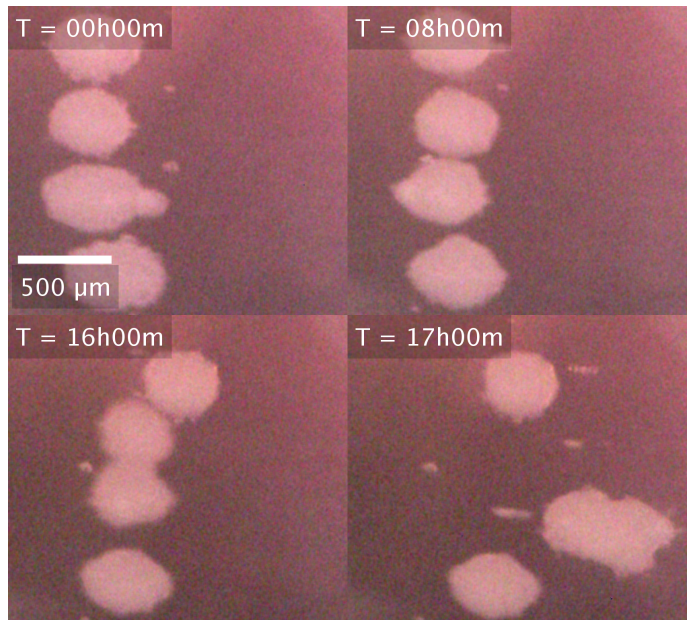


Fig. 15 Manipulation of hMSC spheroids in acoustic levitation. At  $T = 0$ , the spheroids have already moved and the spacing between them has been reduced (See Graphical Abstract for a time-lapse of the process). After 16 h we can see the merging of the two central spheroids. The instability of the new acoustic trap brings the assembloid to the lower node.

approach provides a rapid identification of the best working frequencies and an accurate estimation of the force magnitude applied on the particle from the measurement of the particle velocities.

The high aspect ratio between the ultrasound emitter and the working wavelength assume the use of a one dimensional acoustic model. The spatial distribution of the particle velocities shows an homogeneous radial symmetry (Fig. 4 (b)) along the center axis of the transducer and confirms, as first approximation, the use of plane waves to describe our chip.

As expected by the theory, increasing the cavity height leads to more resonance peaks over the frequency spectrum. Furthermore, the ARF is strong enough, in the case of a light material, to continuously trap, move and maintain the cells or the aggregates over a wide frequency bandwidth, in this study from 1.5 MHz to 2.75 MHz.

The comparison of the frequency resonance inter-spaces between the experimental results and the modelling allows to estimate with accuracy the height dimension of the cavity.

In this article we have reported the design and the characterization of a broadband multi-node standing wave cavity with the ability to trap or move object in a controlled manner. This approach, integrated with other physic or biological aspects, opens the path of large acoustofluidic applications.

The knowledge of the ratio of the maximum to minimum of the acoustic energy density on the working spectrum provides a control lever to adjust the magnitude force applied to the particles. This parameter is essential to flow acoustophoretic applications, like particle focusing or separation.

The possibility to continuously shift the position of each node

allows for example the spatial manipulation of the trapped aggregate but also the direction change of the focus position in a flow configuration<sup>41</sup>. By leaping the frequency, an aggregate of particles could be maintained in the same position with different frequencies.

The use of the 1D acoustic model will be helpful to properly design new setups. This simple model can eventually take into account more complex designs, especially a supplementary layer (a classic transmitter layer, for instance) in the chip.

The proof of concept of a straightforward application has been validated with the merging of two hMSCs spheroids. We show the possibility to handle and to move a column of spheroids, to bring them closer to finally promote their merging. For more accurate manipulation and control of the applied ARF, it is also possible to move the spheroids with a constant force, using the preliminary characterisation of the cavity signature.

This work is the first proof of concept showing that is possible to move and merge cells spheroids in acoustic levitation which is a crucial step for cell therapy and organoids fabrication.

## Conflicts of interest

In accordance with the policy of RSC journals, there are no conflicts of interest to declare.

## Acknowledgements

The authors wish to thank Région Ile-de-France and the DIM ELICIT for their financial support.

## Ethical statement

We declare that all methods in the manuscript were carried out in accordance with relevant guidelines and regulations given by RSC-Lab on a Chip. All procedures involving patients were conducted according to the Helsinki Declaration.

Mesenchymal Stem Cells were isolated from the adipose tissue of a male donor, obtained at Necker-Enfants Malades hospital in Paris, France. The adipose tissue was the surgical leftover and was used for research purposes after a signed consent from the donor and his parents as the legal tutors, according to the French bioethical and medical research regulations. In France, according to the law “loi Jardé” (article L. 1121-1 of the public health code) governing scientific research on human subjects and tissue samples, the surgical leftover can be used for scientific research without the prior approval of an ethical committee.

## Notes and references

- 1 T. Laurell, F. Petersson and A. Nilsson, *Chem. Soc. Rev.*, 2007, **36**, 492–506.
- 2 M. Wiklund, *Lab on a Chip*, 2012, **12**, 2018.
- 3 M. Wu, A. Ozcelik, J. Rufo, Z. Wang, R. Fang and T. Jun Huang, *Microsystems & Nanoengineering*, 2019, **5**, 32.
- 4 J. Friend and L. Y. Yeo, *Reviews of Modern Physics*, 2011, **83**, 647–704.
- 5 F. Petersson, L. Åberg, A.-M. Swård-Nilsson and T. Laurell, *Analytical Chemistry*, 2007, **79**, 5117–5123.
- 6 G. Dumy, M. Hoyos and J.-L. Aider, *The Journal of the Acoustical Society of America*, 2019, **146**, 4557–4568.
- 7 M. Wiklund, J. Toivonen, M. Tirri, P. Hänninen and H. M. Hertz, *Journal of Applied Physics*, 2004, **96**, 1242–1248.
- 8 M. Nordin and T. Laurell, *Lab on a Chip*, 2012, **12**, 4610.
- 9 D. Carugo, T. Octon, W. Messaoudi, A. L. Fisher, M. Carboni, N. R. Harris, M. Hill and P. Glynne-Jones, *Lab Chip*, 2014, **14**, 3830–3842.
- 10 O. Dron, C. Ratier, M. Hoyos and J.-L. Aider, *Microfluidics and Nanofluidics*, 2009, **7**, 857–867.
- 11 P. Augustsson and T. Laurell, *Lab on a Chip*, 2012, **12**, 1742.
- 12 X. Ding, Z. Peng, S.-C. S. Lin, M. Geri, S. Li, P. Li, Y. Chen, M. Dao, S. Suresh and T. J. Huang, *Proceedings of the National Academy of Sciences*, 2014, **111**, 12992–12997.
- 13 N. Jeger-Madiot, L. Arakelian, N. Setterblad, P. Bruneval, M. Hoyos, J. Larghero and J.-L. Aider, *Scientific Reports*, 2021, **11**, 8355.
- 14 M. Evander and J. Nilsson, *Lab on a Chip*, 2012, **12**, 4667.
- 15 A. Lenshof, C. Magnusson and T. Laurell, *Lab on a Chip*, 2012, **12**, 1210.
- 16 J. J. Hawkes and W. T. Coakley, 2001, 10.
- 17 X. Luo, J. Cao, H. Gong, H. Yan and L. He, *Ultrasonics Sonochemistry*, 2018, **48**, 287–298.
- 18 J. Dual and T. Schwarz, *Lab Chip*, 2012, **12**, 244–252.
- 19 J. Hultström, O. Manneberg, K. Dopf, H. Hertz, H. Brismar and M. Wiklund, *Ultrasound in Medicine & Biology*, 2007, **33**, 145–151.
- 20 M. Settnes and H. Bruus, *Physical Review E*, 2012, **85**, 016327.
- 21 R. Barnkob, P. Augustsson, T. Laurell and H. Bruus, *Lab on a Chip*, 2010, **10**, 563.
- 22 S. M. Hagsäter, T. G. Jensen, H. Bruus and J. P. Kutter, *Lab on a Chip*, 2007, **7**, 1336.
- 23 P. Augustsson, R. Barnkob, S. T. Wereley, H. Bruus and T. Laurell, *Lab on a Chip*, 2011, **11**, 4152.
- 24 O. Dron and J.-L. Aider, *EPL (Europhysics Letters)*, 2012, **97**, 44011.
- 25 O. Dron and J.-L. Aider, *Ultrasonics*, 2013, **53**, 1280–1287.
- 26 M. Hill, Y. Shen and J. J. Hawkes, *Ultrasonics*, 2002, **40**, 385–392.
- 27 D. Royer and E. Dieulesaint, *Elastic waves in solids I: Free and guided propagation*, Springer Science & Business Media, 1999.
- 28 H. Bruus, *Lab on a Chip*, 2012, **12**, 1578.
- 29 D. L. Folds and C. D. Loggins, *The Journal of the Acoustical Society of America*, 1977, **62**, 1102–1109.
- 30 J. T. Karlsen and H. Bruus, *Physical Review E*, 2015, **92**, 043010.
- 31 L. V. King, *Proceedings of the Royal Society of London. Series A - Mathematical and Physical Sciences*, 1934, **147**, 212–240.
- 32 T. Hasegawa and K. Yosioka, 6.
- 33 L. Gorkov, author, 1962, p. 773776.
- 34 S. Zhang, C. M. Kube, Y. Song and X. Li, *The Journal of the Acoustical Society of America*, 2016, **140**, EL236–EL241.
- 35 M. W. Widener, *The Journal of the Acoustical Society of America*, 1980, **67**, 1058–1060.

- 36 E. v. K. Hill and D. M. Egle, *The Journal of the Acoustical Society of America*, 1980, **67**, 666–672.
- 37 W. Thielicke and A. Buma, *Ph.D. thesis*, 2014.
- 38 W. Thielicke and E. J. Stadhuis, *Journal of Open Research Software*, 2014, **2**, year.
- 39 Y. Miura, M.-Y. Li, F. Birey, K. Ikeda, O. Revah, M. V. Thete, J.-Y. Park, A. Puno, S. H. Lee, M. H. Porteus and S. P. Paşca, *Nature Biotechnology*, 2020, **38**, 1421–1430.
- 40 H. Cai, Z. Ao, Z. Wu, S. Song, K. Mackie and F. Guo, *Lab on a Chip*, 2021, 10.1039.D1LC00145K.
- 41 M. Kandemir, M. Beelen, R. Wagterveld, D. Yntema and K. Keesman, *Journal of Sound and Vibration*, 2021, **490**, 115723.

## 7 Supplementary materials

By using equation 9, we can write :

$$\begin{aligned}
 F^{rad} &= \frac{4\pi}{3} r_p^3 \left\{ a \frac{\partial \langle p^2 \rangle}{\partial x} - b \frac{\partial \langle v^2 \rangle}{\partial x} \right\} \\
 &= \frac{4\pi}{3} r_p^3 \left\{ a(\rho_w c_w)^2 + b \right\} k v_m^2 \cos(kx + \phi) \sin(kx + \phi) \\
 &= \frac{4\pi}{3} r_p^3 \left\{ a(\rho_w c_w)^2 + b \right\} k v_m^2 \frac{1}{2} \sin(2kx + 2\phi) \\
 &= \frac{4\pi}{3} r_p^3 \left\{ 1 - \frac{\rho_w c_w^2}{\rho_p c_p^2} + 3 \frac{\rho_p - \rho_w}{2\rho_p + \rho_w} \right\} \frac{1}{2} \rho_w k v_m^2 \frac{1}{2} \sin(2kx + 2\phi) \\
 &= \frac{4\pi}{3} r_p^3 \left\{ 1 - \frac{\rho_w c_w^2}{\rho_p c_p^2} + 3 \frac{\rho_p - \rho_w}{2\rho_p + \rho_w} \right\} k E_{ac} \sin(2kx + 2\phi) \\
 &= 4\pi r_p^3 \left\{ \frac{\rho_p + \frac{2}{3}(\rho_p - \rho_w)}{2\rho_p + \rho_w} - \frac{\rho_w c_w^2}{3\rho_p c_p^2} \right\} k E_{ac} \sin(2kx + 2\phi) \\
 &= 4\pi r_p^3 \beta k E_{ac} \sin(2kx + 2\phi)
 \end{aligned} \tag{20}$$

With  $\beta$  the contrast factor.

We define the acoustic energy density as :

$$E_{ac} = \frac{1}{\lambda} \int_0^\lambda \frac{1}{2} \rho_w v(x)^2 dx = \frac{1}{4} \rho_w v_m^2 \tag{21}$$